Electronic Supplementary Information

High performance P-based argyrodite sulfide electrolyte enabled by Sb-based argyrodite doping for all-solid-state lithium metal batteries

Zhihui Ma,[a] Ping Li,*[a] Jie Shi,[a] Feng Sun,[a] Yidi Fu,[a] Zhen Wang,[a] Yixing Fang,[a] Junmei Han,[a] Xuanhui Qu[a]

[a] *Beijing Advanced Innovation Center for Materials Genome Engineering, Institute for Advanced Materials and Technology, University of Science and Technology Beijing, Beijing 100083, PR China*

* Corresponding author.

E-mail address: ustbliping@126.com.

Experimental methods

Materials synthesis

The reagent-grade chemicals of Li_2S (99.9 %, Alfa Aesar), SnS_2 (99.5 %, Energy Chemical), Sb_2S_3 (99.9 %, Aladdin Chemistry. Co., Ltd.), S (99.99%, Sigma-Aldrich), LiI (99.9 %, Alfa Aesar), LiCl (99.9 %, Aladdin Chemistry. Co., Ltd.), and P_2S_5 (99 %, Macklin) were used as starting materials. Specifically, the typical synthetic process was conducted as follows: Firstly, the starting materials were weighed with the specific stoichiometric ratios and sealed into the argon-filled zirconia jars. Then, the precursors were synthesized by ball milling the mixtures at 550 rpm for 24 h, followed by sealing into a quartz tube, and finally annealed at 500 °C for 9 h. The optimized synthesis procedure of LPSC-*x* ($0.0 \leq x \leq 0.1$) samples was carried out as follows: The precursors were obtained by ball milling the mixtures of LSSSI, Li_2S, LiCl and P_2S_5 with the stoichiometric proportions of LPSC-*x* ($0.0 \leq x \leq 0.1$) at 550 rpm for 24 h, LSSSI was obtained as our previous report.[1] The obtained precursors were subsequently sintered at 500 °C for 9 h. The synthesis process of Li_2O-coated $LiNi_{0.8}Co_{0.1}Mn_{0.1}O_2$ (NCM811@Li_2O) cathode was consistent with our previously described method.[2]

Computational methods

Density functional theory (DFT) computations were conducted through the Vienna Ab initio Software Package (VASP 5.4.4) within the Perdew-Burke-Ernzerhof (PBE) generalized gradient approximation and the projected augmented wave (PAW) method.[3-6] The cutoff energy for the plane-wave basis set was set to 450 eV. The Brillouin zone of the surface unit cell was sampled by Monkhorst-Pack (MP) grids with k-point mesh density of $2\pi \times 0.04$ Å^{-1} for further optimization.[7] The convergence criterion for the electronic self-consistent iteration and force was respectively set to 10^{-5} eV and 0.01 eV Å^{-1}. The vacuum layer of 15 Å was introduced to avoid interactions between periodic images.

Materials characterization

The crystalline structures of the samples were determined by X-ray diffraction (XRD) measurements on an X-ray diffractometer (Rigaku Ultima IV) with cooper Kα radiation (λ = 1.54178 Å). The test SSEs were sealed in an airtight holder covering with Kapton polyimide films. The Phenom XL G2

scanning electron microscope fitted with energy-dispersive spectroscopy (EDS) was employed to investigate the morphologies and elemental compositions of samples. The Raman spectra of SSEs were obtained utilizing a Renishaw Invia Raman spectrometer under an excitation wavelength of 532 nm. XPS measurements were conducted by means of a Thermo Scientific ESCALab 250Xi instrument with Al Kα radiation. Rietveld refinements for the XRD data were carried out through the Fullprof software.

Electrochemical characterization

The conductivities of the synthesized samples were determined by the electrochemical impedance spectra (EIS). The powder samples were loaded into a PEEK mold (diameter: 10 mm) using two stainless-steel (SUS) disks as blocking electrodes, then compressed into a tablet (thickness: ~0.75 mm) under 300 MPa at ambient temperature. EIS measurements were conducted on a CHI660C electrochemical workstation (Shanghai Chenhua) in the frequency range between 0.01 and 10 MHz with an applied amplitude of 10 mV. To evaluate the electronic conductivity of SSEs, the DC polarization method was performed on the SUS/SSEs/SUS cell at 30 ℃. The SUS/SSEs/SUS cell was assembled using abovementioned process: the powder samples were cold pressed into pellets (thickness: 0.75 mm) at a pressure of 300 MPa with two stainless-steel (SUS) rods serving as blocking electrodes. The Li/SSEs/Li symmetric batteries were fabricated as follows: 130 mg of SSEs powders were cold-pressed by 275 MPa to form the SSEs interlayer in the PEEK mold. Lithium foils (diameter: 10 mm, thickness: 0.15 mm) were attached to both sides of SSEs interlayer, and then pressed under 75 MPa. The NEWARE CT-4008 battery-test system was used to test the Li plating/stripping properties of the assembled Li-Li symmetric cells at 30 °C. To assess the electrochemical stability of SSEs, the cyclic voltammetry (CV) measurement was performed via the cell configuration of C-SSEs/SSEs/Li at 30 °C. The C-SSEs/SSEs/Li was fabricated as follows. 125 mg of SSEs were first loaded into a PEEK mold and compressed by 300 MPa to form the SSEs interlayer. ~10.0 mg of the composite electrode materials (with a 7:3 mass ratio of SSEs to super P) was then spread on the surface of SSEs layer, followed by pressing under 200 MPa. Li foil was subsequently pressed on the other side of the

electrolyte layer under 75 MPa. CV was carried out within a wide potential range from 0 to 7 V at a scanning rate of 0.5 mV s^{-1}. For the fabrication of ASSLMBs, 125 mg of SSEs were first loaded into a PEEK mold (diameter: 10 mm) and compressed by 300 MPa to form the SSEs interlayer. The composite cathode was prepared by mixing 105.0 mg of the active material (NCM811@Li_2O powder) and 45.0 mg of SSEs samples at a mass ratio of 7:3. Then 10.0 ± 0.1 mg of the composite cathode (corresponding to an active material loading mass of ~8.9 mg cm^{-2} (i.e., 8.9 ± 0.1 mg cm^{-2})) was weighed and homogeneously spread on the surface of SSEs layer, followed by pressing under 200 MPa. Li foil was subsequently pressed on the other side of the electrolyte layer under 75 MPa. The electrochemical performances of the assembled cells were measured on a NEWARE CT-4008 battery-test system in the potential range from 2.6 to 4.4 V (*vs.* Li/Li^+) at 30 °C (1C = 170 mA g^{-1}).

Air stability test

For the H_2S generation measurements, 100 mg of pelletized SSEs, a fan, a thermohygrometer (THM-01, Delixi Electric) and a H_2S sensor (BH-4M, Bosean electronic) were sealed in an airtight container filled with moist air (~28% RH, 25 °C). The amount of H_2S released from the SSEs was collected via the H_2S sensor. After exposure to humid air under ~28% RH for 60 min, the structure and ionic conductivity variations of SSEs were studied by XRD, Raman and EIS measurements. To assess the electrochemical cycling performance stability of SSEs upon air exposure, the ASSLBs coupling the as-synthesized/air-exposed SSEs layer and NCM811@Li_2O cathode layer with Li-In anode layer were constructed following the assembled procedure of ASSLMBs described above. The electrochemical performances of ASSLBs with an active material loading mass of 8.92 mg cm^{-2} were also tested on a NEWARE CT-4008 battery-test system at 30 °C (1C = 170 mA g^{-1}).

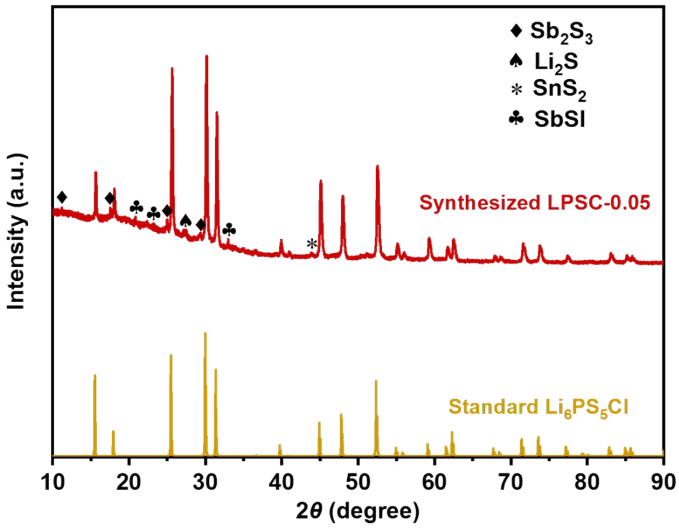

Fig. S1. X-ray diffraction pattern of the obtained LPSC-0.05 sample via the typical synthetic process.

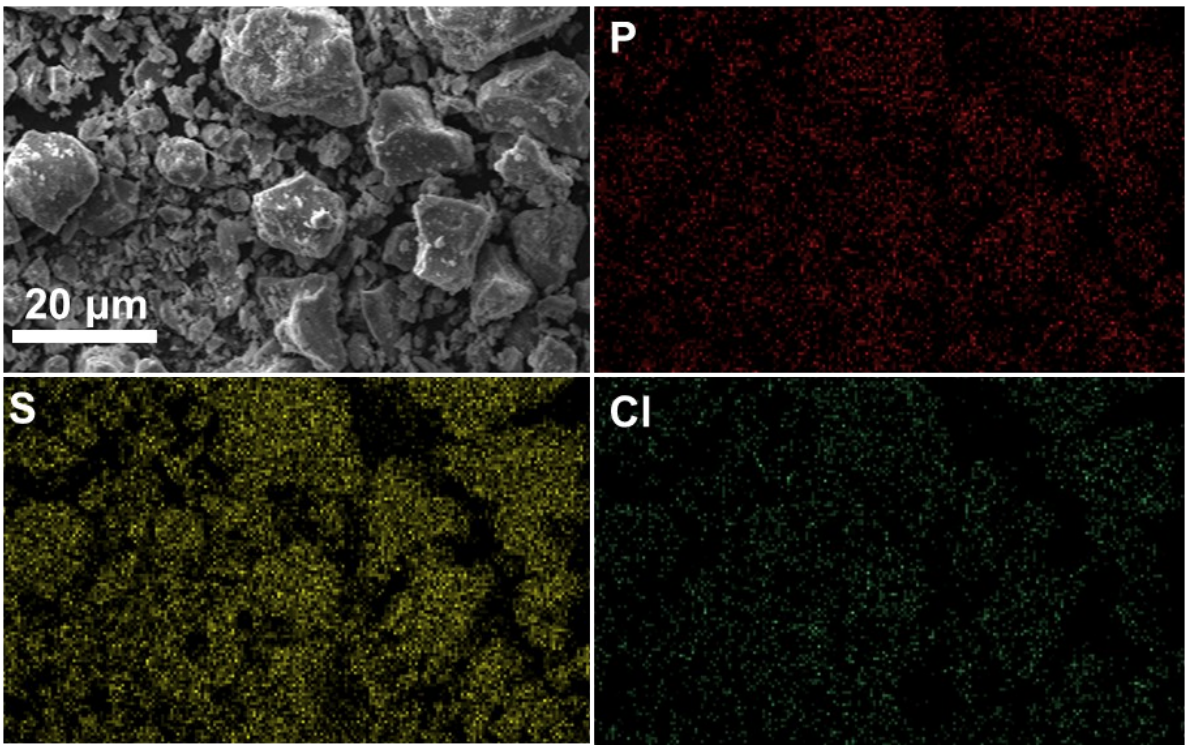

Fig. S2. SEM and corresponding EDS elemental mapping images of LPSC-0 electrolyte through the two-step annealing approach.

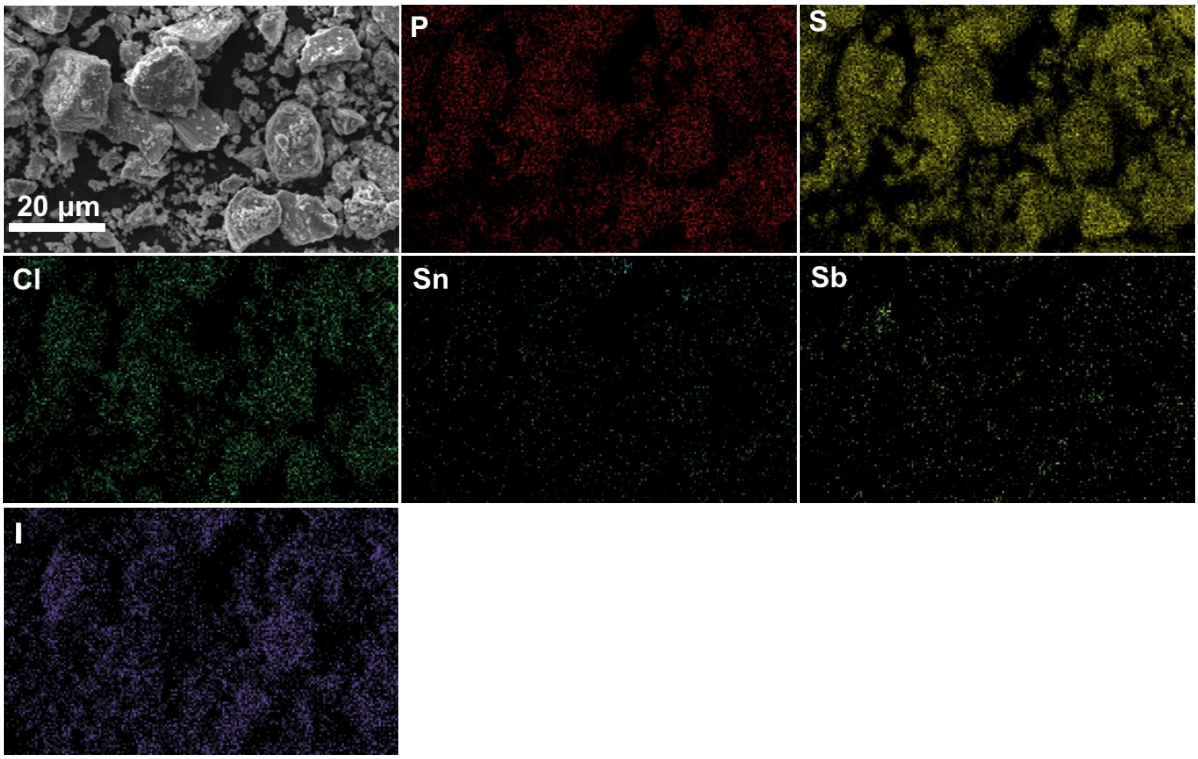

Fig. S3. SEM and corresponding EDS elemental mapping images of LPSC-0.05 through the two-step annealing strategy.

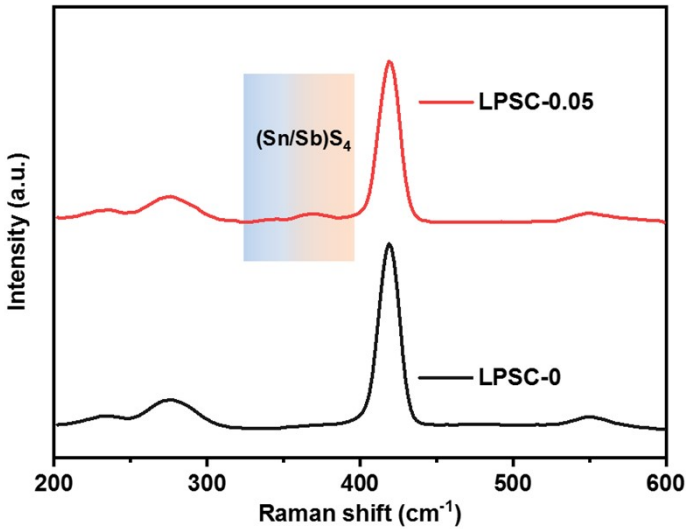

Fig. S4. Raman spectra of LPSC-0 and LPSC-0.05 samples.

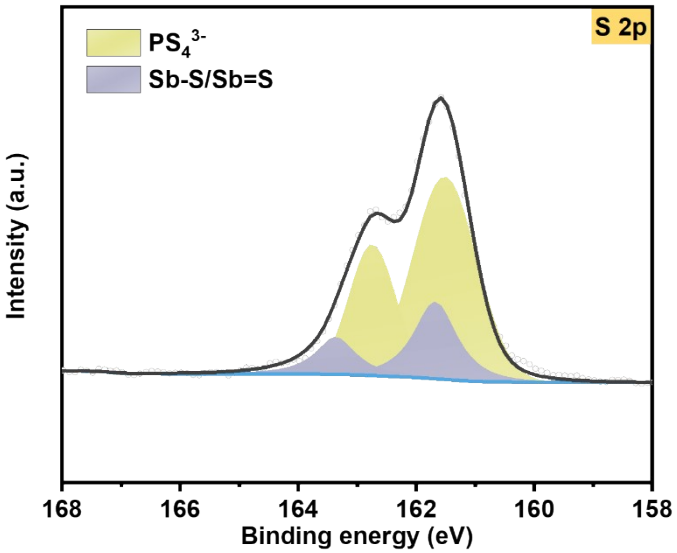

Fig. S5. S 2p XPS spectrum of LPSC-0.05 electrolyte.

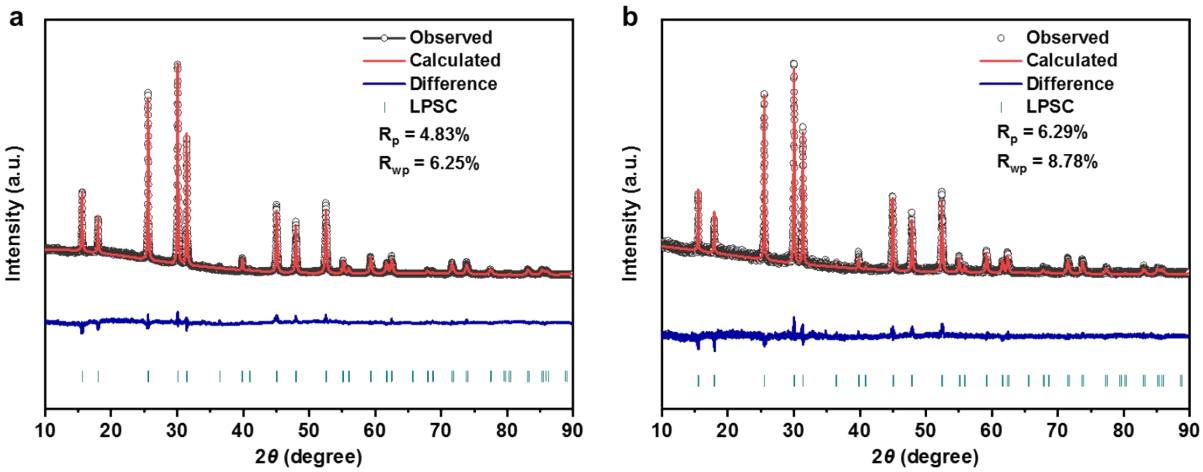

Fig. S6. Rietveld analysis of LPSC-0 and LPSC-0.03 samples.

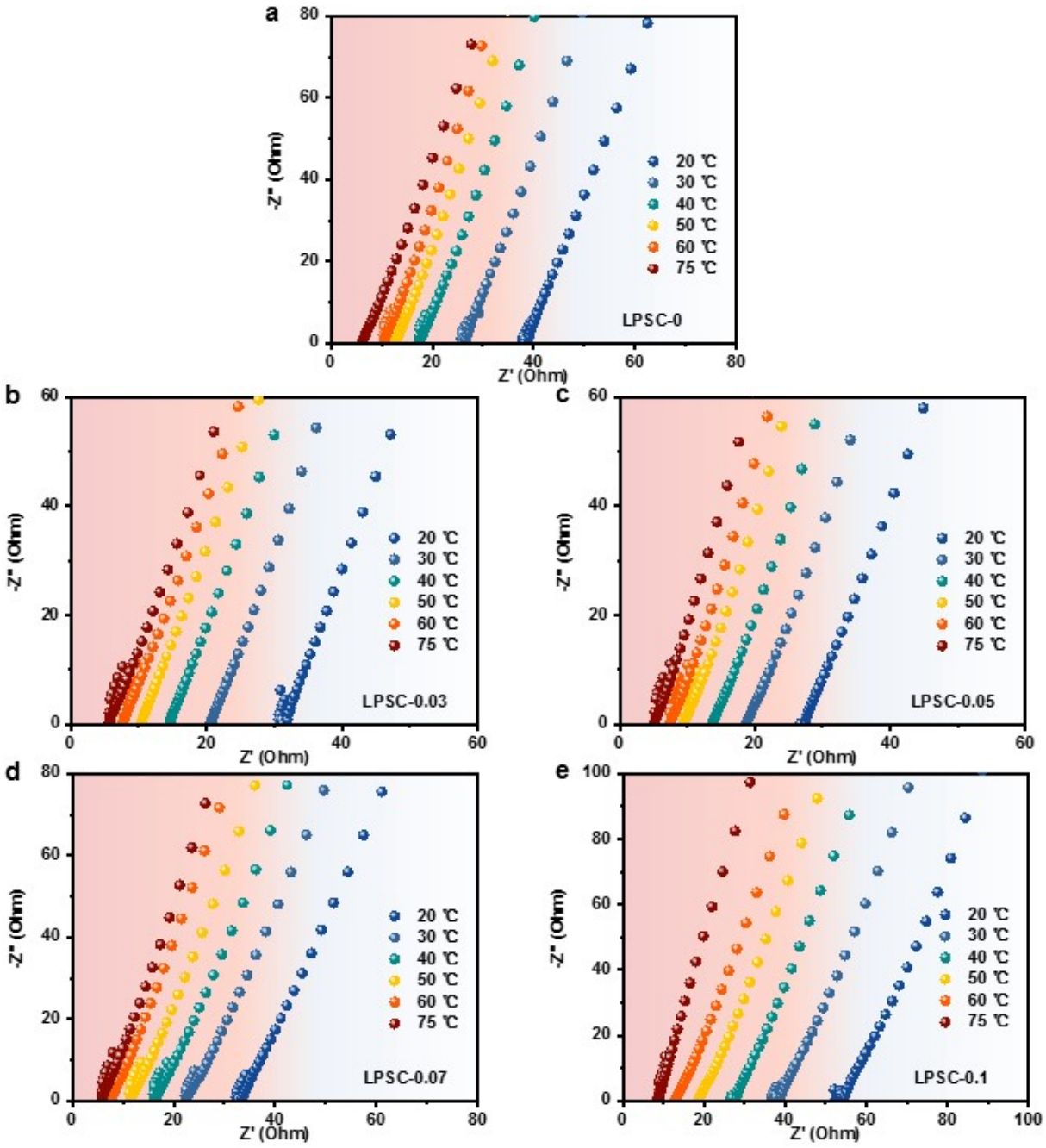

Fig. S7. Nyquist plots of LPSC-*x* ($0.0 \leq x \leq 0.1$) samples at a temperature range from 20 to 75 °C.

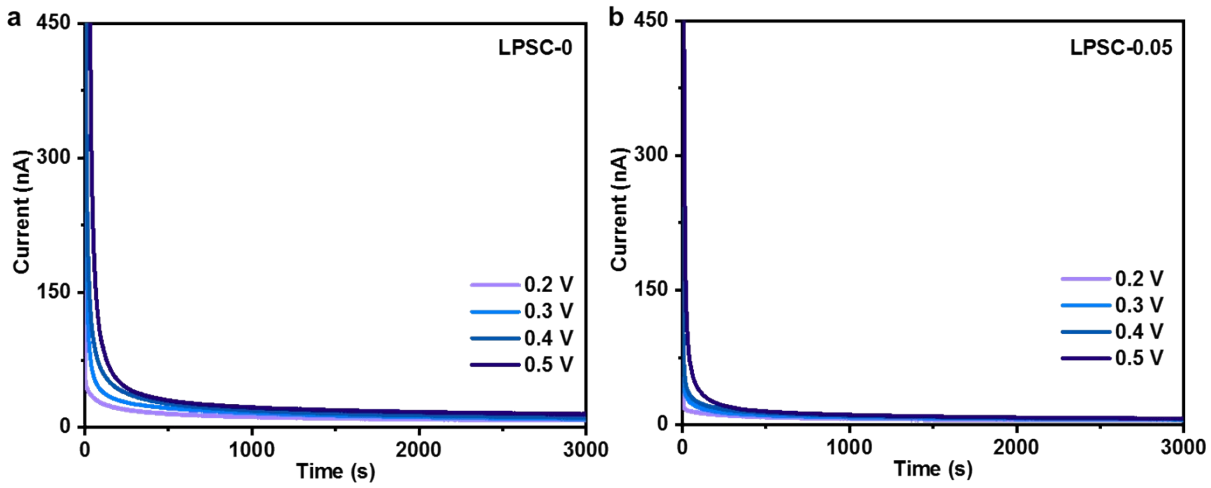

Fig. S8. DC polarization profiles of SUS/LPSC-0/SUS and SUS/LPSC-0.05/SUS cells at 0.2~0.5 V.

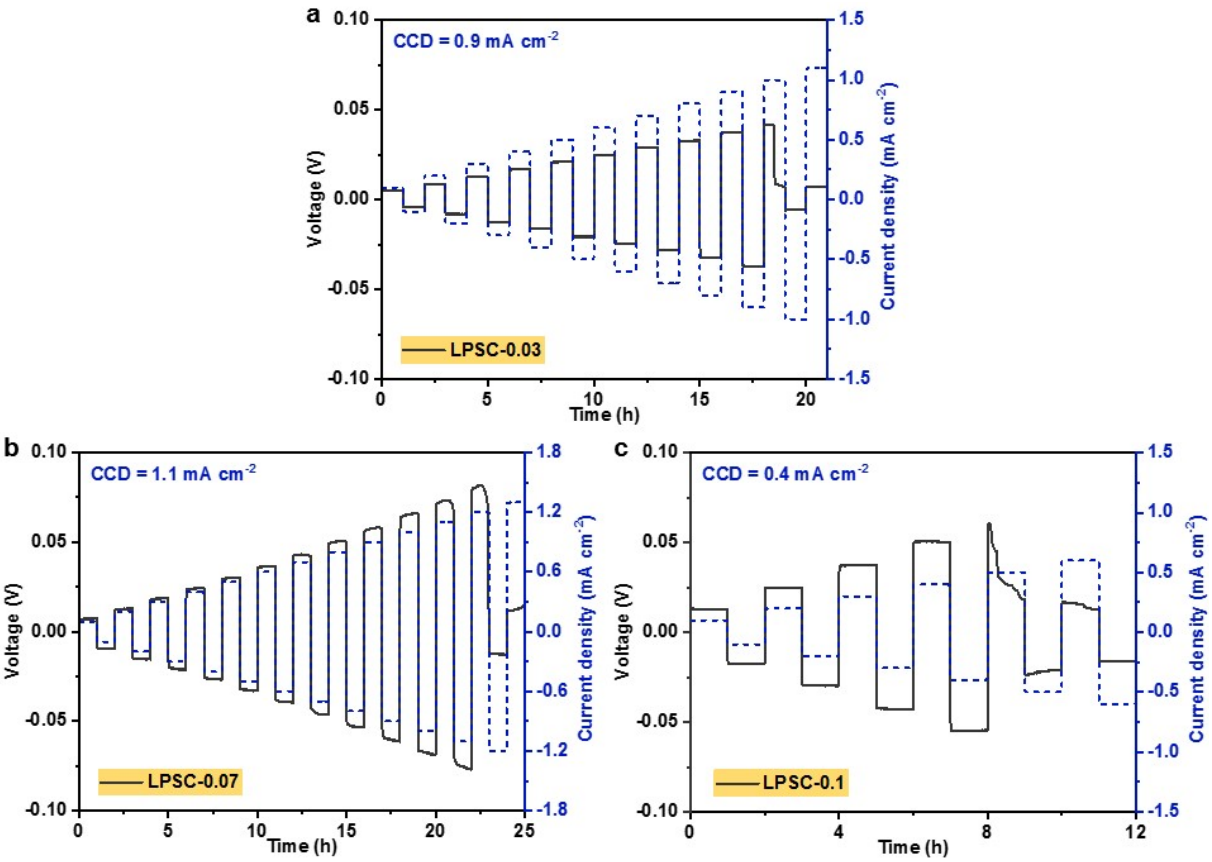

Fig. S9. Galvanostatic cycling of the (a) Li/LPSC-0.03/Li, (b) Li/LPSC-0.07/Li and (c) Li/LPSC-0.1/Li symmetric cells at a step-elevated current density of 0.1 mA cm^{-2} at 30 °C.

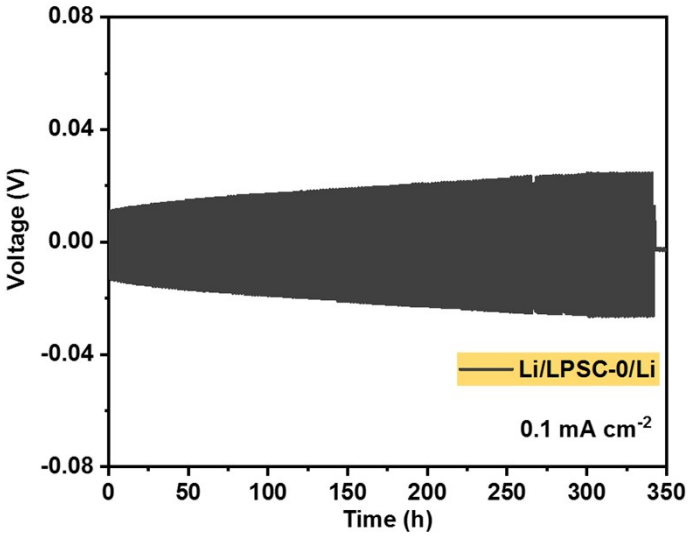

Fig. S10. Time dependence of voltage curves during galvanostatic Li plating/stripping for Li/LPSC-0/Li symmetric cell.

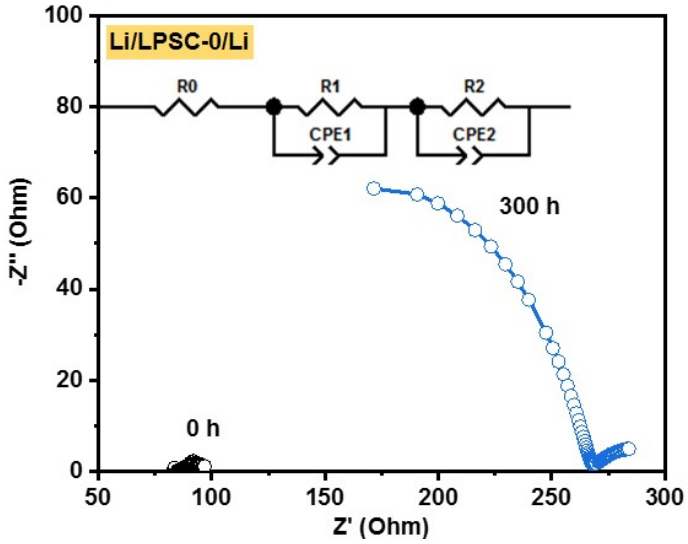

Fig. S11. Nyquist plots of the Li/LPSC-0/Li symmetric cell before and after galvanostatic cycling at a current density of 0.1 mA cm^{-2} (inset is the equivalent circuit diagram for impedance fitting).

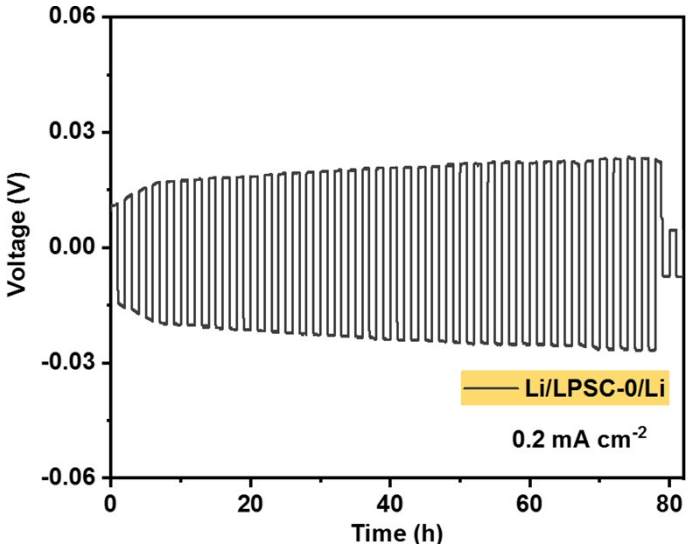

Fig. S12. Galvanostatic cycling performance of Li/LPSC-0/Li symmetric cell at 0.2 mA cm^{-2}.

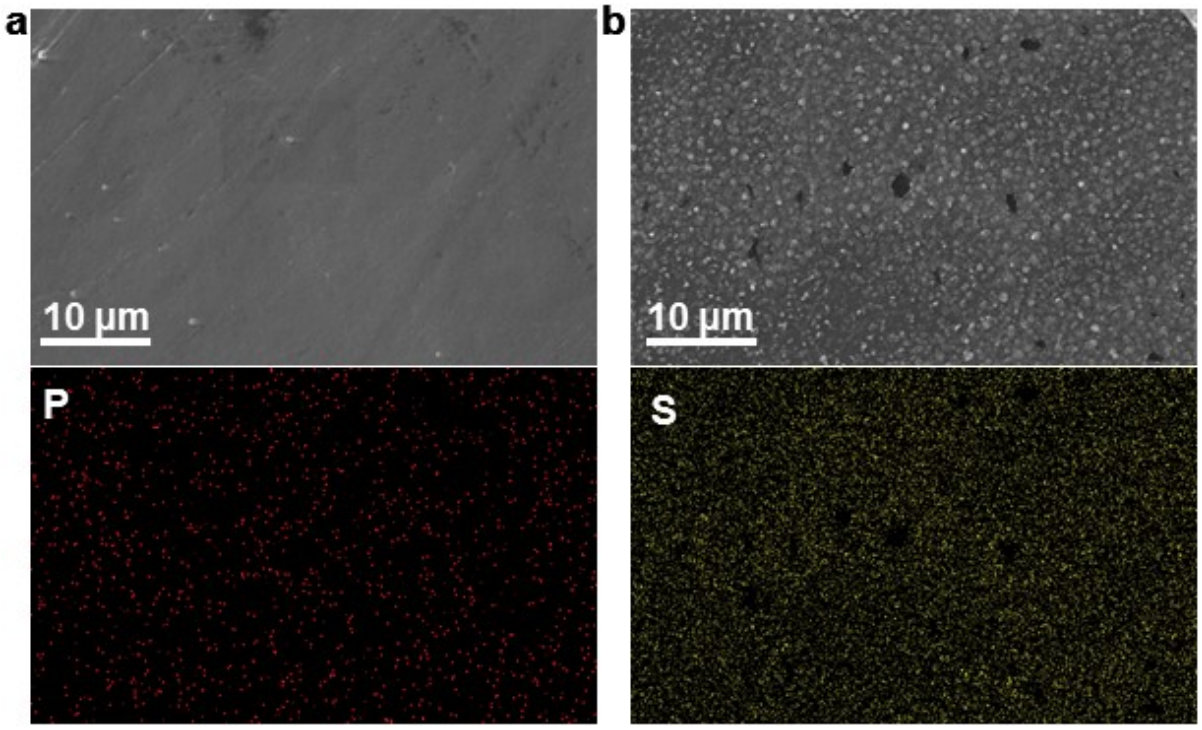

Fig. S13. (a) SEM image of the pristine lithium metal; (b) The SEM and corresponding EDS element mapping images of the Li surface at Li/LPSC-0 interface after 96h cycling at a current density of 0.1 mA cm^{-2}.

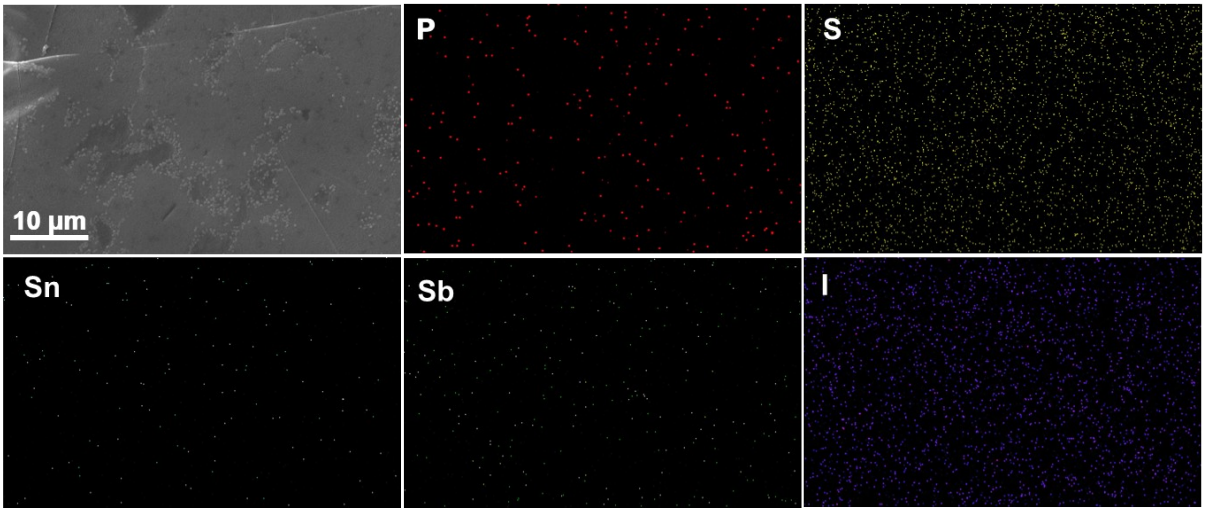

Fig. S14. The morphology and corresponding element distribution images of the Li surface in the Li/LPSC-0.05/Li cell after Li plating/stripping at 0.1 mA cm^{-2} for 96 h.

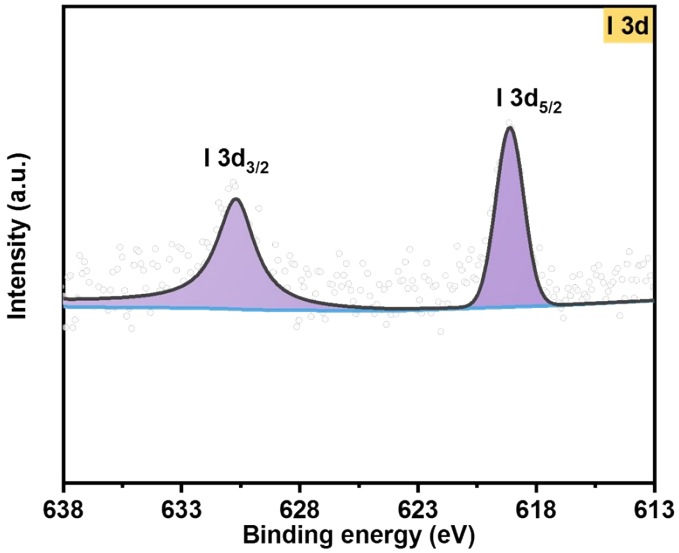

Fig. S15. I 3d XPS spectrum at the Li metal surface after Li plating/stripping at 0.1 mA cm^{-2} for 96 h.

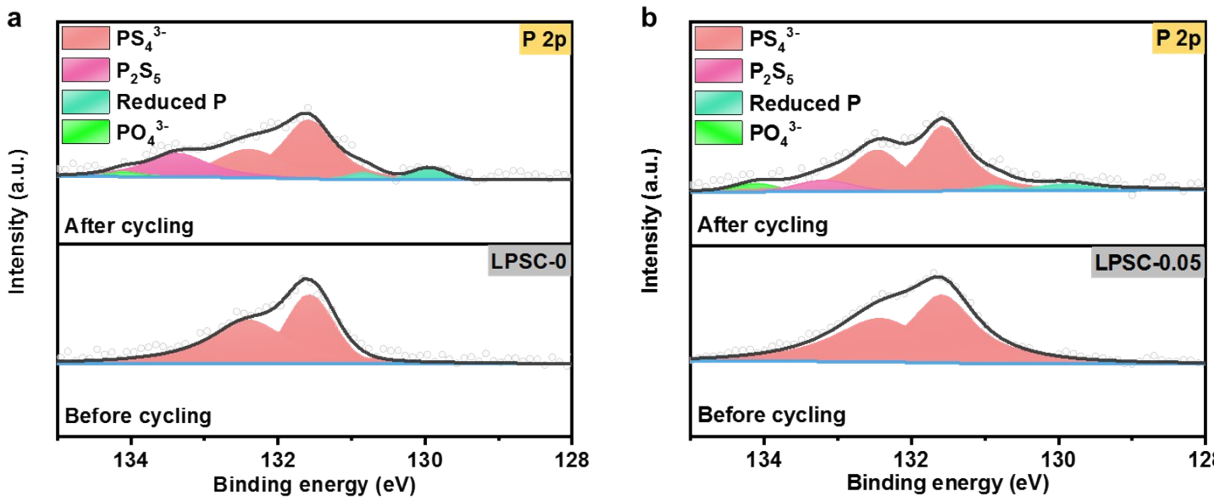

Fig. S16. The comparative P 2p XPS spectra of lithium symmetric cells at (a) Li/LPSC-0 and (b) Li/LPSC-0.05 interfaces before and after cycling for 96 h at 0.1 mA cm^{-2}.

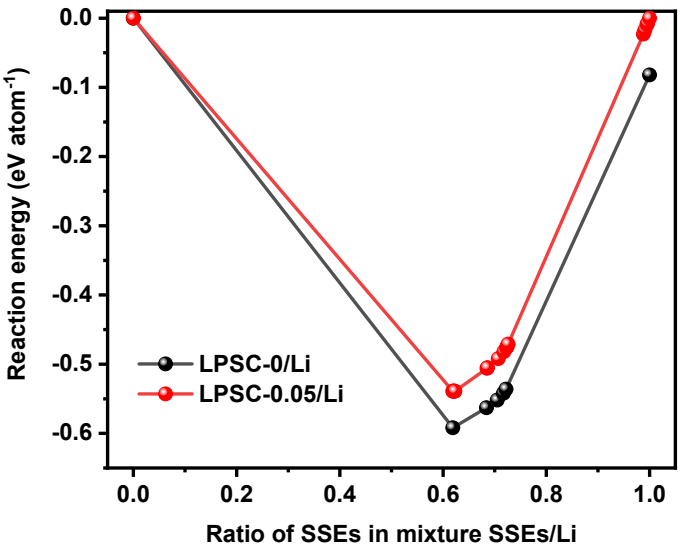

Fig. S17. Calculated reaction energies of LPSC-0/Li and LPSC-0.05/Li interfaces.

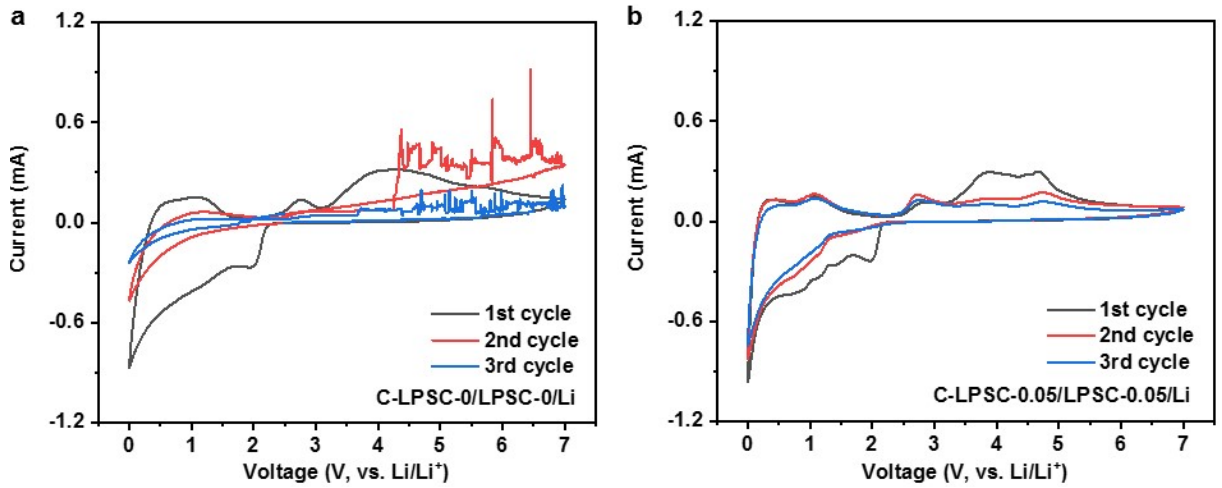

Fig. S18. Cyclic voltammetry curves of (a) C-LPSC-0/LPSC-0/Li and (b) C-LPSC-0.05/LPSC-0.05/Li cells measured in a voltage range of 0~7 V.

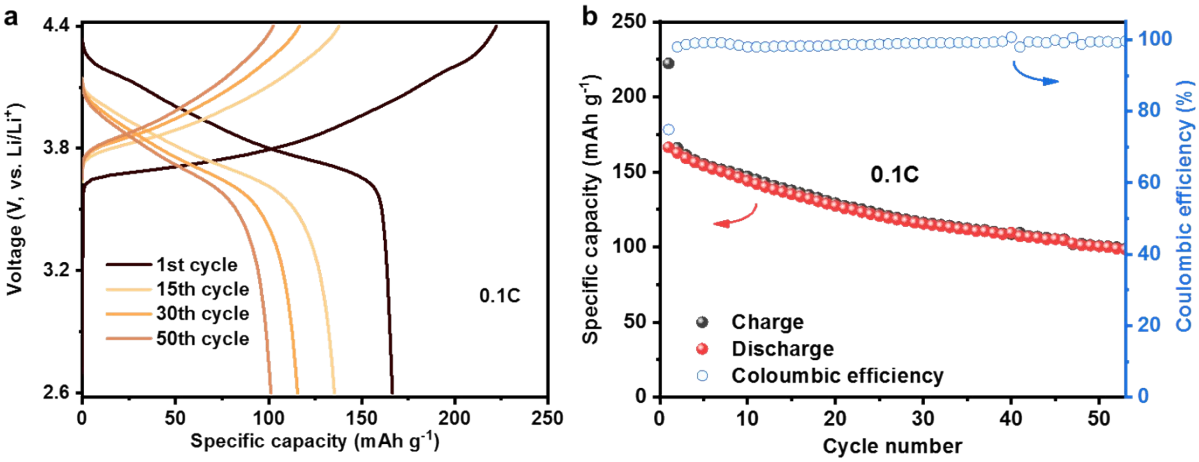

Fig. S19. (a) Galvanostatic charge and discharge curves of NCM811@Li_2O/LPSC-0/Li battery at 0.1C; (b) Galvanostatic cycling performance and corresponding Coulombic efficiency of the ASSLMBs at 0.1C.

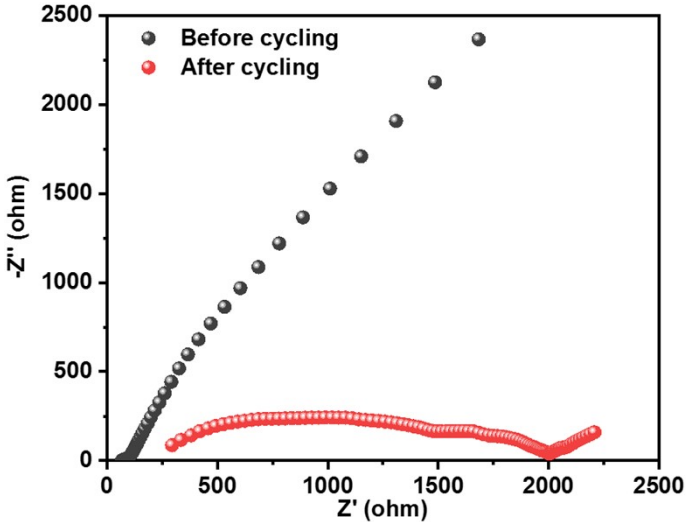

Fig. S20. Nyquist plots of the NCM811@Li_2O/LPSC-0.05/Li cell before and after cycling at 0.1C.

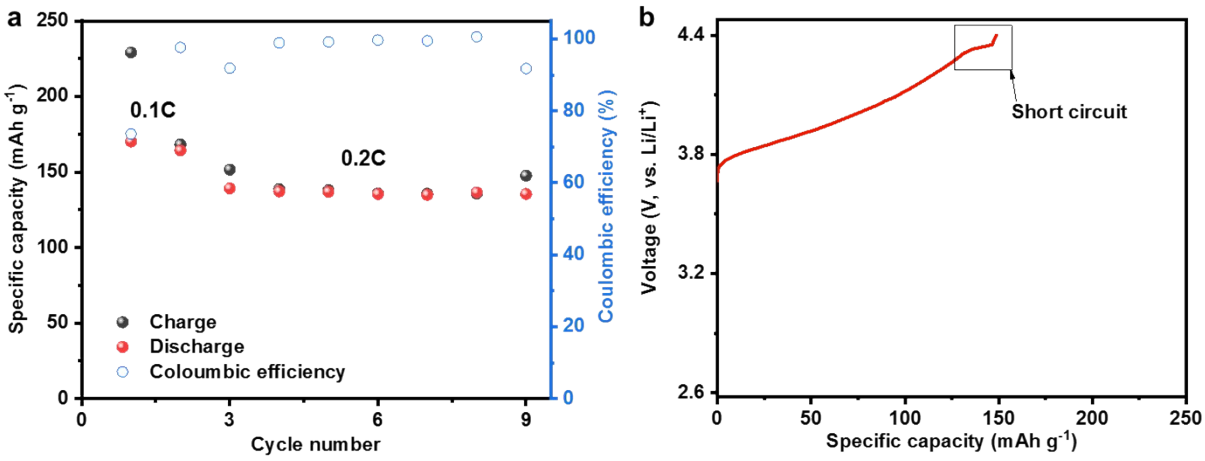

Fig. S21. (a) Cycling stability of NCM811@Li_2O/LPSC-0/Li battery at 0.2C; (b) Galvanostatic charge voltage profile of the ASSLMBs at 9th cycle.

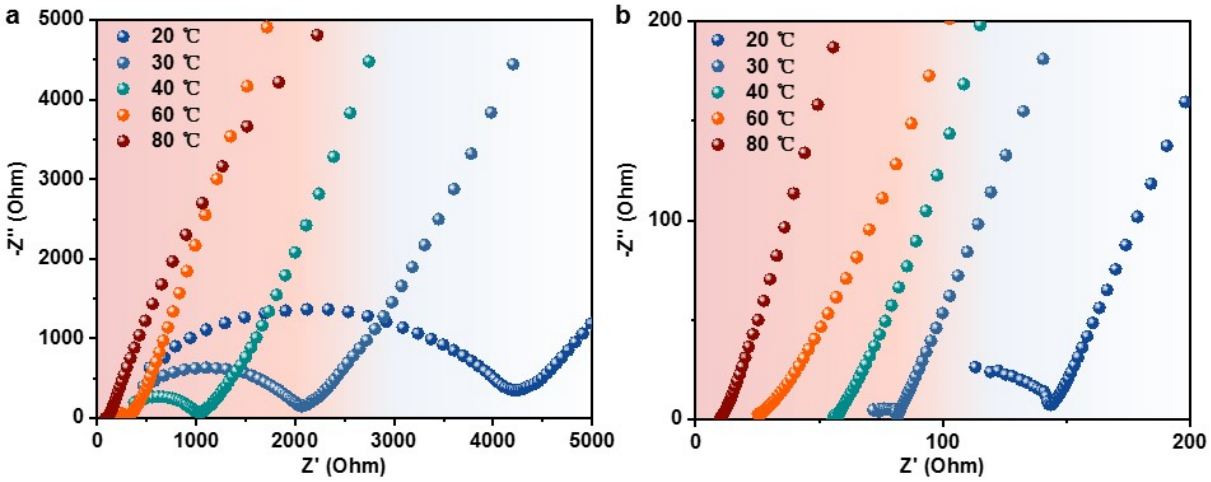

Fig. S22. Impedance spectra of the air-exposed (a) LPSC-0 and (b) LPSC-0.05 samples at a temperature range from 20 to 80 °C.

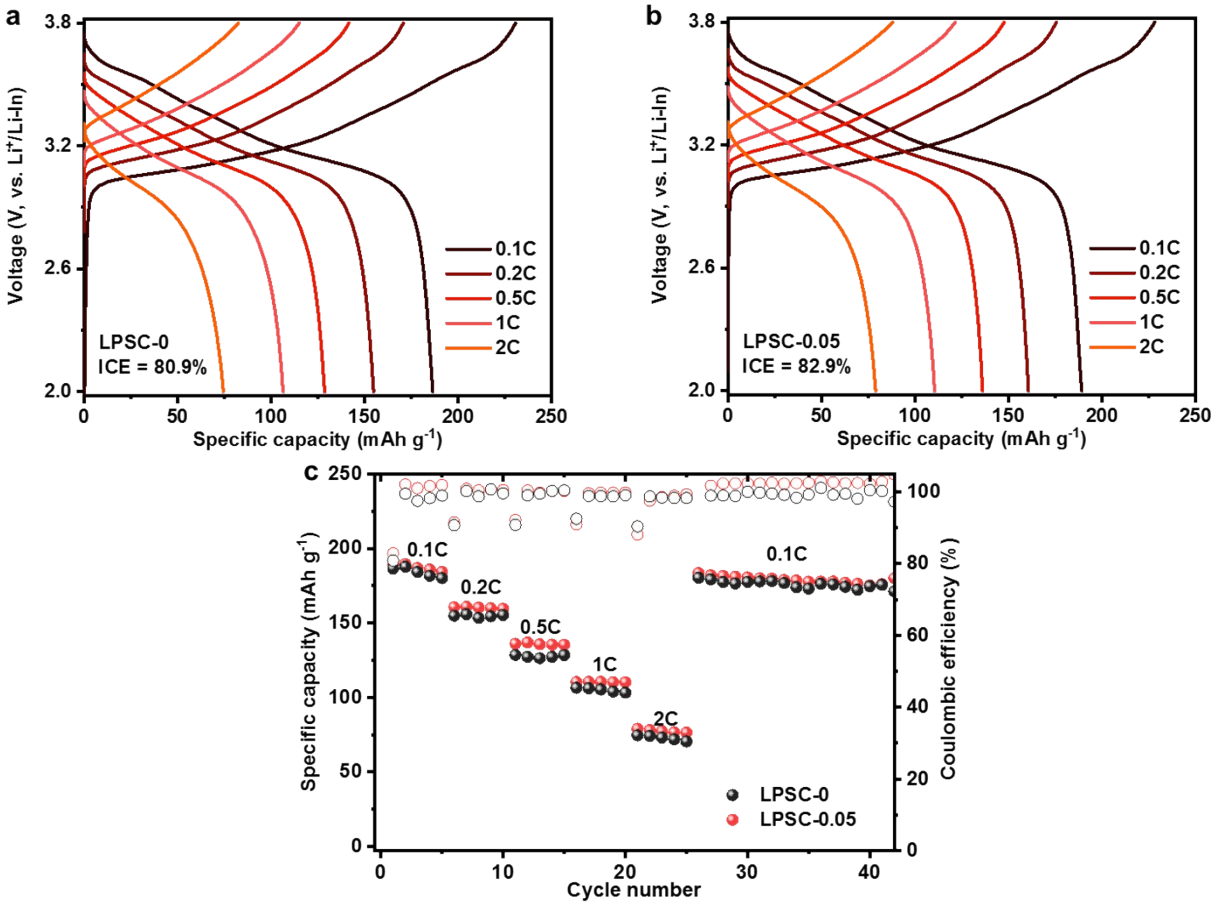

Fig. S23. Typical charge and discharge curves of (a) NCM811@Li_2O/LPSC-0/Li-In and (b) NCM811@Li_2O/LPSC-0.05/Li-In batteries at various current densities. (c) Comparison of the rate capability of the ASSLBs with the as-synthesized LPSC-0 and LPSC-0.05 electrolytes.

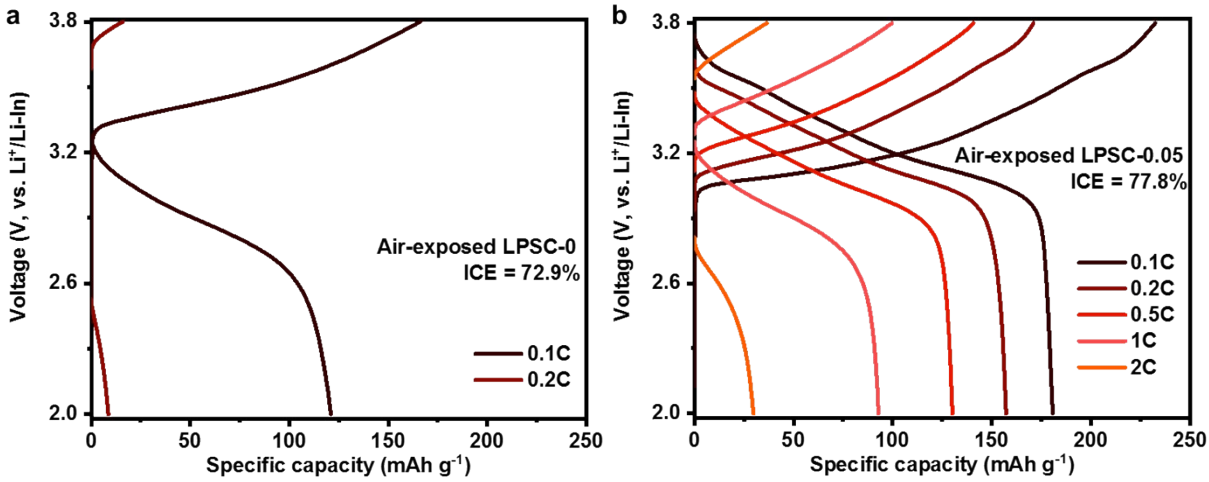

Fig. S24. Galvanostatic charge and discharge profiles of the ASSLBs with (a) air-exposed LPSC-0 electrolyte and (b) air-exposed LPSC-0.05 electrolyte at various current densities.

Table S1. Rietveld analysis results of LPSC-0 with space group *F*4*m*.

$a = b = c = 9.85071$Å, $R_p = 4.83\%$, $R_{wp} = 6.25\%$					
Atom	Wyckoff site	*x*	*y*	*z*	Occupancy
P1	4b	0.0	0.0	0.5	1
Cl1	4a	0.0	0.0	1.0	0.383
Cl2	4d	0.25	0.25	0.75	0.617
Li1	48h	0.32020	0.01830	0.67980	0.5
S1	4d	0.25	0.25	0.75	0.383
S2	16e	0.12011	-0.12011	0.62009	1
S3	4a	0.0	0.0	1.0	0.617

Table S2. Rietveld analysis results of LPSC-0.03 with space group *F*4*m*.

$a = b = c = 9.91105$ Å; $R_p = 6.29\%$; $R_{wp} = 8.78\%$					
Atom	Wyckoff site	*x*	*y*	*z*	Occupancy
P1	4b	0.0	0.0	0.5	0.973
Sb1	4b	0.0	0.0	0.5	0.016
Sn1	4b	0.0	0.0	0.5	0.011
Cl1	4a	0.0	0.0	1.0	0.372
Cl2	4d	0.25	0.25	0.75	0.598
I1	4a	0.0	0.0	1.0	0.019
I2	4d	0.25	0.25	0.75	0.011
Li1	48h	0.31843	0.01614	0.70889	0.501
S1	4d	0.25	0.25	0.75	0.383
S2	16e	0.12011	-0.12011	0.62009	1
S3	4a	0.0	0.0	1.0	0.617

Table S3. Rietveld analysis results of LPSC-0.05 with space group *F*4*m*.

$a = b = c = 9.96732$ Å; $R_p = 5.82\%$; $R_{wp} = 7.39\%$					
Atom	Wyckoff site	*x*	*y*	*z*	Occupancy
P1	4b	0.0	0.0	0.5	0.955
Sb1	4b	0.0	0.0	0.5	0.027
Sn1	4b	0.0	0.0	0.5	0.018
Cl1	4a	0.0	0.0	1.0	0.364
Cl2	4d	0.25	0.25	0.75	0.586
I1	4a	0.0	0.0	1.0	0.031
I2	4d	0.25	0.25	0.75	0.019
Li1	48h	0.31843	0.01614	0.70889	0.502
S1	4d	0.25	0.25	0.75	0.383
S2	16e	0.12011	-0.12011	0.62009	1
S3	4a	0.0	0.0	1.0	0.617

Table S4. Comparison of the SSEs-based Li symmetric cell performance.

Composition	Critical current density [mA cm^{-2}]	Cycling current density [mA cm^{-2}]	Cycle Time [h]	Temperature [°C]	Reference
$Li_{6.988}P_{2.994}Nb_{0.2}S_{10.934}O_{0.6}$	-	0.1	100	RT	8
$Li_{3.2}P_{0.8}Sn_{0.2}S_4$	-	0.1	600	RT	9
$Li_{4.1}P_{0.9}Sn_{0.1}S_4I$	1.1	0.1	1500	25	10
Li_6PS_5Cl	0.5	0.1	158	25	11
$Li_6Sb_{0.075}P_{0.925}S_5Cl$	1.2	0.1 0.5	800 400	25	11
$Li_{5.5}P_{0.9}Sn_{0.1}S_{4.2}O_{0.2}Cl_{1.6}$	1.2	0.5	200	RT	12
$Li_{6.04}P_{0.98}Bi_{0.02}S_{4.97}O_{0.03}Cl$	1.1	0.1 1.0	600 200	RT	13
$Li_{5.6}PS_{4.6}ClBr_{0.4}$	0.35	0.2	500	RT	14
$Li_{6.05}P_{0.95}Zr_{0.05}S_{4.9}O_{0.1}Cl$	1.7	0.1 0.5	800 400	RT	15
LPSC-0.05	**1.4**	**0.1** **0.5**	**6000** **500**	**30**	**This work**

where RT stands for room temperature.

Table S5. Comparison of the physicochemical properties of the LPSC-0.05 electrolyte with other reported SSEs

Composition	Ionic conductivity [S cm^{-1}]	Electronic conductivity [S cm^{-1}]	E_a [eV]	Moisture stability	Reference
$Li_{10}GeP_2S_{12}$	1.2×10^{-2}	9.0×10^{-9}	24 kJ mol^{-1}	☹	16
$Li_{10}SnP_2S_{12}$	3.8×10^{-3}	7.0×10^{-9}	0.23	☹	17
Li_3PS_4	2.6×10^{-4}	1.1×10^{-8}	0.31	☹	10
$Li_{4.1}P_{0.9}Sn_{0.1}S_4I$	1.8×10^{-3}	6.9×10^{-9}	0.27	☺	10
$Li_{3.875}Sn_{0.875}As_{0.125}S_4$	1.4×10^{-3}	1.5×10^{-9}	0.21	☺	18
$Li_{6.4}Sn_{0.4}Sb_{0.6}S_5I$	3.5×10^{-4}	8.0×10^{-8}	0.31	☺	1
Li_6PS_5Cl	2.4×10^{-3}	7.6×10^{-9}	0.32	☹	11
$Li_6Sb_{0.075}P_{0.925}S_5Cl$	3.6×10^{-3}	6.5×10^{-9}	0.25	☺	11
$Li_{6.1}Cu_{0.1}P_{0.9}S_5Cl$	4.3×10^{-3}	1.5×10^{-9}	0.25	☺	19
LPSC-0.05	**5.2×10^{-3}**	**2.0×10^{-9}**	**0.25**	☺	**This work**

References

1 Z. Ma, J. Shi, D. Wu, D. Chen, S. Shang, X. Qu and P. Li, *J. Mater. Chem. A*, 2023, **11**, 23342.

2 J. Shi, P. Li, K. Han, D. Sun, W. Zhao, Z. Liu, G. Liang, K. Davey, Z. Guo and X. Qu, *Energy Storage Mater.*, 2022, **51**, 306.

3 J. P. Perdew, K. Burke and M. Ernzerhof, *Phys. Rev. Lett.*, 1996, **77**, 3865.

4 B. Hammer, L. B. Hansen and J. K. Nørskov, *Phys. Rev. B*, 1999, **59**, 7413.

5 P. E. Blöchl, *Phys. Rev. B*, 1994, **50**, 17953.

6 G. Kresse and D. Joubert, *Phys. Rev. B*, 1999, **59**, 1758.

7 H. J. Monkhorst and J. D. Pack, *Phys. Rev. B*, 1976, **13**, 5188.

8 N. Ahmad, L. Zhou, M. Faheem, M. K. Tufail, L. Yang, R. Chen, Y. Zhou and W. Yang, *ACS Appl. Mater. Interfaces*, 2020, **12**, 21548.

9 F. Zhao, S. H. Alahakoon, K. Adair, S. Zhang, W. Xia, W. Li, C. Yu, R. Feng, Y. Hu, J. Liang, X. Lin, Y. Zhao, X. Yang, T.-K. Sham, H. Huang, L. Zhang, S. Zhao, S. Lu, Y. Huang and X. Sun, *Adv. Mater.*, 2021, **33**, 2006577.

10 L. Zhang, G. Liu, N. Zhang, H. Yu and X. Yao, *ACS Appl. Energy Mater.*, 2024, **7**, 4565.

11 H. Liu, Q. Zhu, Y. Liang, C. Wang, D. Li, X. Zhao, L. Gao and L.-Z. Fan, *Chem. Eng. J.*, 2023, **462**, 142183.

12 G. Li, S. Wu, H. Zheng, Y. Yang, J. Cai, H. Zhu, X. Huang, H. Liu and H. Duan, *Adv. Funct. Mater.*, 2023, **33**, 2211805.

13 H. Liu, Q. Zhu, C. Wang, G. Wang, Y. Liang, D. Li, L. Gao and L.-Z. Fan, *Adv. Funct. Mater.*, 2022, **32**, 2203858.

14 Y. Subramanian, R. Rajagopal and K.-S. Ryu, *J. Power Sources*, 2022, **520**, 230849.

15 D. Wang, H. Shi, W. Cui, H. Li, J. Niu, S. Wang and Z. Xu, *J. Mater. Chem. A*, 2024, **12**, 10863.

16 N. Kamaya, K. Homma, Y. Yamakawa, M. Hirayama, R. Kanno, M. Yonemura, T. Kamiyama, Y. Kato, S. Hama, K. Kawamoto and A. Mitsui, *Nat. Mater.*, 2011, **10**, 682.

17 Z. Jiang, Z. Li, X. Wang, C. Gu, X. Xia and J. Tu, *ACS Appl. Mater. Interfaces*, 2021, **13**, 30739.

18 G. Sahu, Z. Lin, J. Li, Z. Liu, N. Dudney and C. Liang, *Energy Environ. Sci.*, 2014, **7**, 1053.

19 B. W. Taklu, W.-N. Su, Y. Nikodimos, K. Lakshmanan, N. T. Temesgen, P.-X. Lin, S.-K. Jiang, C.-J. Huang, D.-Y. Wang, H.-S. Sheu, S.-H. Wu and B. J. Hwang, *Nano Energy*, 2021, **90**, 106542.